Computations of fully nonlinear three-dimensional wave–wave and wave–body interactions. Part 1. Dynamics of steep three-dimensional waves

By MING XUE†, HONGBO XÜ‡, YUMING LIU
AND DICK K. P. YUE

Department of Ocean Engineering, Massachusetts Institute of Technology, Cambridge,
MA 02139, USA

We develop an efficient high-order boundary-element method with the mixed-Eulerian–Lagrangian approach for the simulation of fully nonlinear three-dimensional wave–wave and wave–body interactions. For illustration, we apply this method to the study of two three-dimensional steep wave problems. (The application to wave–body interactions is addressed in an accompanying paper: Liu, Xue & Yue 2001.) In the first problem, we investigate the dynamics of three-dimensional overturning breaking waves. We obtain detailed kinematics and full quantification of three-dimensional effects upon wave plunging. Systematic simulations show that, compared to two-dimensional waves, three-dimensional waves generally break at higher surface elevations and greater maximum longitudinal accelerations, but with smaller tip velocities and less arched front faces. For the second problem, we study the generation mechanism of steep crescent waves. We show that the development of such waves is a result of three-dimensional (class II) Stokes wave instability. Starting with two-dimensional Stokes waves with small three-dimensional perturbations, we obtain direct simulations of the evolution of both L_2 and L_3 crescent waves. Our results compare quantitatively well with experimental measurements for all the distinct features and geometric properties of such waves.

1. Introduction

Steep overturning three-dimensional waves are ubiquitous in the ocean environment. The dynamics of such waves are of importance in the consideration of extreme slamming loads and wave over-topping on ships and marine structures, energy and momentum transfer from surface waves to currents, and turbulence mixing of the upper marine layer. The understanding and modelling of three-dimensional steep or breaking waves is thus of fundamental and practical interest in ocean science and engineering.

In this paper, we develop an effective and robust computational capability based on a mixed-Eulerian–Lagrangian (MEL) approach using a high-order boundary element method to simulate fully nonlinear three-dimensional wave–wave and wave–body interactions. To illustrate the usefulness of the method and to understand steep

† Currently with Salomon Smith Barney, New York, USA.
‡ Currently with Shell Development Co., Houston, USA.

three-dimensional wave dynamics, we apply the numerical method to study two three-dimensional steep wave problems: (*a*) the dynamics of three-dimensional wave breaking; and (*b*) the nonlinear mechanism for the development of crescent waves. The application of this method to nonlinear wave–body problems is considered in an accompanying paper: Liu, Xue & Yue (2001).

For wave breaking, existing experimental and computational studies tend to be mainly for the two-dimensional problem (see Rapp & Melville 1990 for a review of experiments; and Banner & Peregrine 1993, and Tsai & Yue 1996 for reviews of numerical simulations). For simulation of steep two-dimensional waves, a seminal work was Longuet-Higgins & Cokelet (1976), who developed the mixed-Eulerian–Lagrangian (MEL) approach using a boundary-integral equation (BIE) formulation. Since then, a number of improvements/extensions have been made, notably Vinje & Brevig's (1981) development of the Cauchy-integral formulation and Dold's (1992) treatment of time evolution terms. The understanding of two-dimensional breaking waves was improved by New, McIver & Peregrine (1985) who performed detailed computations, Dommermuth *et al.* (1988) who obtained quantitative comparisons to breaking wave measurements in a tank, Yao, Wang & Tulin (1994) who considered wave-group dynamics; and Longuet-Higgins & Dommermuth (1997) who examined the role of crest instabilities.

Despite these advances, the fundamental issue of how and why a wave breaks remains an open question (see e.g. Longuet-Higgins 1996). A number of different criteria for the onset of wave breaking have been suggested. Examining breaking of waves due to converging sidewalls, submerged disturbances, and wave focusing, Schultz, Huh & Griffin (1994) suggested that the root-mean-square potential energy rather than the classical wave steepness is a better and more reliable criterion. The generality of this criterion appears to be limited, however, since it is known that, in some cases, details of an initial profile perturbation (which does not substantially change the potential energy) may determine whether the wave subsequently develops into either an overturning or non-breaking wave (e.g. Longuet-Higgins & Dommermuth 1997). (The present simulation of three-dimensional crescent waves offers another example, see §5.2.) From modulated wave groups, Yao *et al.* (1994) observed that waves start to break when the particle velocity at the crest exceeds the wave group velocity. The generalization of this criterion is not easy since the group velocity is not well defined for general nonlinear waves. Based on the breaking behaviour of modulated wave trains, Banner & Tian (1998) found a threshold for the rate of half-wavelength-averaged momentum and energy, which can be used to separate breaking from recurrence of steep waves. The application of this criterion to general wave fields is also not straightforward. Generalization of these two-dimensional results to three-dimensional waves has not been achieved. For irregular waves, Snyder & Kennedy (1983) used the vertical-acceleration criterion to develop a geometro-statistical model for white caps. But, the threshold value of the free-surface vertical acceleration is determined empirically without basic understanding of the wave-breaking process.

Reliable results for truly three-dimensional problems are still relatively rare (e.g. Isaacson 1982; Romate 1989). Simulations to date have not been completely successful, primarily because of limitations on accuracy/resolution which also affect stability, and computational efficiency and power. In this paper, we extend MEL/BIE to three dimensions using a high-order quadratic boundary-element method (QBEM). A problem of immediate interest is the dynamics of three-dimensional overturning waves. Following Longuet-Higgins & Cokelet (1976), we start with plane progressive

Stokes waves (fundamental wavelength L) but now apply briefly a three-dimensional surface pressure (of transverse wavelength W). Varying the ratio $\gamma \equiv W/L$ over a broad range, we perform high-resolution simulations of plunging waves with different degrees of three-dimensionality. From these simulations, we obtain the detailed wave kinematics and quantify the three-dimensional effects on the kinematics. Analysis of the results in the late stages of wave overturning shows that a condition corresponding to free fall obtains in portions of the plunging tip as evidenced by the vanishing of normal surface accelerations (relative to gravity) in these regions. Under such free-fall conditions, accurate simulation becomes difficult and sensitive to (small) numerical errors, leading eventually to the numerical breakdown of the simulations.

A second steep three-dimensional wave problem of much interest is the often observed phenomenon of regularly distributed crescent-shaped wave patterns in the open ocean (Kinsman 1984; Shrira, Badulin & Kharif 1996) and in laboratory basins (Su *et al.* 1982; Su 1982). Results on the mechanisms for the development of such waves still appear inconclusive. Su *et al.* (1982) speculated that such waves result from three-dimensional (class II) instability of Stokes waves; while Saffman & Yuen (1980) and Meiron, Saffman & Yuen (1982) assumed the crescent wave patterns to be steady three-dimensional bifurcations of Stokes waves. Recently, Shrira *et al.* (1996) added non-conservative effects into the model Zakharov equation and obtained a qualitative prediction of the persistent asymmetric pattern. In any event, since these theories are based either on linear stability analysis or on weakly nonlinear model equations, it is unlikely that quantitative comparisons to crescent waves in experiments (which tend to be quite steep) can be obtained.

In this work, we carry out direct simulations of three-dimensional crescent waves starting from steep two-dimensional Stokes waves with small class II (three-dimensional) unstable perturbations (according to McLean 1982). Following the fully non-linear evolutions, we obtain, depending on the initial perturbations, fully featured 1:2 sub-harmonic (L_2) and 1:3 sub-harmonic (L_3) crescent waves. Significantly, detailed crescent features and geometry obtained in the simulations compare quantitatively well with experimental wave basin measurements. These simulations show that the formation of crescent waves is directly (and possibly solely) a result of fully nonlinear three-dimensional evolution of unstable Stokes waves.

The paper is organized as follows. In §2, the initial boundary-value problem as well as the associated MEL/BIE formulation for general wave–wave and wave–body interaction problems are presented. In §3, the development and implementation of three-dimensional MEL using QBEM is outlined and select validation tests of the method are presented. In §4, we perform a systematic numerical study of the dynamics of three-dimensional breaking waves. The study of crescent wave generation is in §5. We conclude in §6.

2. Mathematical formulation

We consider the general interaction problem of steep waves, with or without the presence of a (floating) body, in the context of fully nonlinear free-surface potential flow. The hydrodynamic problem is formulated as an initial boundary-value problem for the velocity potential which we solve using a mixed-Eulerian–Lagrangian (MEL) approach employing a high-order boundary-integral-equation (BIE) method.

Cartesian coordinates $\mathbf{x} = (x, y, z)$ fixed in space are chosen with the origin at the undisturbed water level, x and y being the two horizontal directions, and z the vertical direction, positive upward. For a given characteristic length scale L, all

variables hereafter are non-dimensionalized by further choosing time and mass units such that the density of water ρ and the gravity acceleration g are both unity.

2.1. *The initial boundary-value problem (IBVP)*

The flow is described by a velocity potential $\phi(x, t)$ which, for continuity, satisfies the Laplace equation,

$$\nabla^2 \phi(x, t) = 0, \qquad x \in \mathscr{V}(t), \tag{2.1}$$

where t is time, and $\mathscr{V}(t)$ the fluid domain. On a prescribed impervious boundary, $\mathscr{B}(t)$, the normal velocity of the flow equals that of the boundary:

$$\frac{\partial \phi}{\partial n} = \phi_n = U(x, t) \cdot n, \qquad x \in \mathscr{B}(t), \tag{2.2}$$

where n is the unit normal out of $\mathscr{B}(t)$ and U the prescribed velocity of $\mathscr{B}(t)$. On the free surface, $\mathscr{F}(t)$, the dynamic boundary condition can be written in Lagrangian form:

$$\frac{\mathrm{D}\phi}{\mathrm{D}t} = \tfrac{1}{2}|\nabla\phi|^2 - z - P_{\mathscr{F}}, \qquad x \in \mathscr{F}(t), \tag{2.3}$$

where $\mathrm{D}/\mathrm{D}t \equiv \partial/\partial t + \nabla\phi \cdot \nabla$ denotes material derivative and $P_{\mathscr{F}}$ the (given) pressure on $\mathscr{F}(t)$. The kinematic boundary condition on $\mathscr{F}(t)$ in Lagrangian form is

$$\frac{\mathrm{D}x}{\mathrm{D}t} = \nabla\phi, \qquad x \in \mathscr{F}(t). \tag{2.4}$$

For deep water, the appropriate far-field condition is

$$\nabla\phi(x, t) \to 0 \qquad \text{as} \quad z \to -\infty. \tag{2.5}$$

At initial time, $t = 0$, the free-surface position $\mathscr{F}(0)$ and the velocity potential on the free surface $\phi(x \in \mathscr{F}(0))$ are given, while $\mathscr{B}(t)$ and $U(x \in \mathscr{B}(t), t)$ are presumed given (or can be solved) for all t. The IBVP is complete with the imposition of appropriate radiation conditions in the far field.

2.2. *The mixed-Eulerian–Lagrangian (MEL) approach*

At any time t, given $\mathscr{B}(t)$ and $U(x \in \mathscr{B}(t), t)$, and $\mathscr{F}(t)$ and $\phi(x \in \mathscr{F}(t), t)$, the boundary-value problem for ϕ satisfying (2.1) is a generalized Cauchy problem whose solution is completely determined in terms of values on the boundary only. This lends itself to a BIE formulation of the MEL approach. This solution procedure involves two main steps:

I. Given $\mathscr{B}(t)$, $\phi_n(x \in \mathscr{B})$, $\mathscr{F}(t)$ and $\phi(x \in \mathscr{F})$, solve the boundary-value problem (BVP) for $\phi_n(x \in \mathscr{F})$, and in particular obtain the velocity $\nabla\phi(x \in \mathscr{F})$.

II. Integrate in time the kinematic and dynamic free-surface boundary conditions (2.4) and (2.3) for $\mathscr{F}(t + \Delta t)$ and $\phi(x \in \mathscr{F}(t + \Delta t))$. Repeat the process.

The approach has three important characteristics: (i) the linear BVP is solved in step I with the actual (time-exact) boundary at that time step; (ii) the integration of the nonlinear boundary conditions in time in step II is explicit; and (iii) only boundary values of the unknown (ϕ and ϕ_n) are involved on account of the elliptic field equation (2.1). As can be expected, computation time and storage are generally dominated by step I; while computational complexities, associated for example with stability of the nonlinear free-surface boundary conditions, are mainly confined to step II.

2.3. *BIE formulation of the BVP*

To formulate the BVP into a BIE, we introduce the Rankine (free-space) Green function, $G(\boldsymbol{x}, \boldsymbol{x}') = 1/r$, where $r \equiv |\boldsymbol{x} - \boldsymbol{x}'|$ and $\boldsymbol{x}' \equiv (x', y', z')$ is the source point. Applying Green's second identity to ϕ and G and taking the limit $\boldsymbol{x} \to \partial \mathscr{V}$, where $\partial \mathscr{V}$ is the boundary of $\mathscr{V}$, we obtain the requisite BIE:

$$\alpha(\boldsymbol{x})\phi(\boldsymbol{x}) + \iint_{\partial \mathscr{V}} [\phi(\boldsymbol{x}')G_n(\boldsymbol{x}, \boldsymbol{x}') - \phi_n(\boldsymbol{x}')G(\boldsymbol{x}, \boldsymbol{x}')] \, \mathrm{d}S(\boldsymbol{x}') = 0, \quad \boldsymbol{x} \in \partial \mathscr{V}, \qquad (2.6)$$

where the Cauchy principal part of the singular integral is assumed here and hereafter. In (2.6), the interior solid angle $\alpha(\boldsymbol{x})$ can be evaluated by

$$\alpha(\boldsymbol{x}) = - \iint_{\partial \mathscr{V}} G_n(\boldsymbol{x}, \boldsymbol{x}') \, \mathrm{d}S(\boldsymbol{x}'), \qquad (2.7)$$

which is obtained from (2.6) with a constant ϕ. For $\boldsymbol{x} \in \mathscr{B}/\mathscr{F}$, the Neumann/Dirichlet boundary condition is applied, and (2.6) is a Fredholm integral equation of the second/first kind.

After obtaining the solution on the boundary from (2.6), the solution in the whole flow field can be evaluated using

$$\phi(\boldsymbol{x}) = \frac{1}{4\pi} \iint_{\partial \mathscr{V}} [\phi_n(\boldsymbol{x}')G(\boldsymbol{x}, \boldsymbol{x}') - \phi(\boldsymbol{x}')G_n(\boldsymbol{x}, \boldsymbol{x}')] \, \mathrm{d}S(\boldsymbol{x}'), \quad \boldsymbol{x} \in \mathscr{V}, \qquad (2.8)$$

for the velocity potential, and

$$\nabla \phi(\boldsymbol{x}) = \frac{1}{4\pi} \iint_{\partial \mathscr{V}} [\phi_n(\boldsymbol{x}')\nabla_x G(\boldsymbol{x}, \boldsymbol{x}') - \phi(\boldsymbol{x}')\nabla_x G_n(\boldsymbol{x}, \boldsymbol{x}')] \, \mathrm{d}S(\boldsymbol{x}'), \quad \boldsymbol{x} \in \mathscr{V}, \qquad (2.9)$$

for the velocity.

2.4. *Far-field boundary conditions*

As pointed out earlier, the proper formulation of the IBVP requires some specification of boundary conditions in the far field. In this paper, our interest is in nonlinear dynamics of periodic three-dimensional waves. Thus we impose doubly periodic boundary conditions in the two horizontal dimensions. In this case, the BIE domain is greatly reduced by introducing the doubly periodic Green function G^p which satisfies, for a periodic domain of dimensions L by W:

$$G^p(x - x', y - y', z - z') = G^p(x + mL - x', y + nW - y', z - z'), \qquad (2.10)$$

for any integers m, n. The domain of the BIE (2.6) is then simply $\mathscr{F} \cup \mathscr{B}$ in a single periodic domain. The doubly periodic Green function G^p can be written as a double sum of Rankine sources:

$$G^p = \sum_{m=-\infty}^{\infty} \sum_{n=-\infty}^{\infty} \left\{ [(x + mL - x')^2 + (y + nW - y')^2 + (z - z')^2]^{-1/2} \right.$$
$$\left. - [(mL)^2 + (nW)^2]^{-1/2} \right\} + \frac{2\pi z}{LW}, \qquad (2.11)$$

where the last term is included to ensure $\nabla G^p \to 0$ as $z \to -\infty$. For the evaluation of G^p in (2.11), efficient summation formulas are available (Breit 1991; Newman 1992).

2.5. *Conservation of mass and energy*

Global accuracy of the numerical scheme can be checked for conservation of mass and energy. For mass conservation, the Gauss condition must be satisfied:

$$\iint_{\partial \mathscr{V}} \phi_n \, \mathrm{d}S = 0. \tag{2.12}$$

Alternatively, in the vertical direction in the absence of a body, the mean water level must be invariant:

$$\bar{z} \equiv \iint_{\mathscr{F}} z n_z \, \mathrm{d}S = \text{constant} \tag{2.13}$$

where n_z is the z-component of $\boldsymbol{n}$ (of $\mathscr{F}$).

If no energy is added to the flow, the total energy of the fluid is invariant. If work is done by an imposed pressure $P_{\mathscr{F}}$ on $\mathscr{F}$ or body motion on $\mathscr{B}$, the rate of change of the total energy is equal to the imposed work done:

$$\frac{\mathrm{d}}{\mathrm{d}t}(E_k + E_p) = - \iint_{\mathscr{F} \cup \mathscr{B}} p \phi_n \, \mathrm{d}S, \tag{2.14}$$

where p is the fluid pressure given by the Bernoulli equation, and E_k and E_p are respectively the kinetic and potential energies:

$$E_k = \frac{1}{2} \iint_{\partial \mathscr{V}} \phi \phi_n \, \mathrm{d}S \quad \text{and} \quad E_p = \frac{1}{2} \iint_{\partial \mathscr{V}} z^2 n_z \, \mathrm{d}S. \tag{2.15}$$

3. Numerical method

We address here key issues associated with the numerical implementation of the MEL/BIE method. In addition, we present convergence tests and results that illustrate the accuracy/resolution of the method.

3.1. *Solution of the BIE*

As pointed out earlier, the success of the MEL approach for practical computations depends very much on the efficacy of the BIE solver for the BVP. Existing BIE solvers commonly employ piecewise-constant approximations for the unknowns, piecewise-linear approximation of the boundary, and collocation at panel centroids (see e.g. Hess & Smith 1964). This so-called 'constant-panel' method (CPM) has a number of shortcomings for the present problem. First, the quadratic convergence of CPM with panel size $\Delta \ell$ is too slow/expensive for accurate three-dimensional simulations. Secondly, at intersections of the free surface ('$\mathscr{F}$' or Dirichlet) and body ('$\mathscr{B}$' or Neumann) boundaries, CPM fails to converge with decreasing $\Delta \ell$, in general, if the boundary slopes are discontinuous (see Xü & Yue 1992). Thirdly, robust treatment of the $\mathscr{F} \cap \mathscr{B}$ intersection generally requires collocation at the intersection itself (see e.g. Lin, Newman & Yue 1984; Dommermuth *et al.* 1988) which however is incompatible with CPM.

To circumvent the above, higher-order panel or BIE methods must be sought. After a systematic study of higher-order panels including super- and sub-parametric elements (order of the geometry representation respectively higher and lower than that for the boundary unknowns), we selected finally an iso-parametric quadratic boundary-element method (QBEM). In QBEM, we employ a piecewise bi-quadratic representation of both $\partial \mathscr{V}$, and ϕ and ϕ_n on $\partial \mathscr{V}$. The boundary panels are now curvilinear quadrilaterals or (degenerate) curvilinear triangles with nine and seven nodes

respectively where boundary positions, and ϕ and ϕ_n values are specified/collocated. QBEM now obtains quadratic convergence with $\Delta\ell$ even in the presence of $\mathscr{F} \cap \mathscr{B}$ intersections with discontinuous boundary slopes. Furthermore, boundary nodes at panel edges provide a robust treatment of boundary intersections. Significantly, for a given minimax (relative) error, say $O(10^{-3})$, QBEM is some two orders of magnitude more efficient than CPM for general applications. The efficiency and accuracy of the present MEL/BIE implementation is to a large extent a result of the efficacy of QBEM. Details of the QBEM implementation and performance can be found in Xü (1992) and Xü & Yue (1992) and are not repeated here.

Upon discretization/collocation of (2.6), we obtain a linear algebraic system which is in general dense, non-symmetric and, because of the first-kind equations on $\mathscr{F}$, not diagonally dominant. For $O(N)$ boundary unknowns, direct solution of the system via Gauss elimination requires $O(N^3)$ effort. For the three-dimensional problems we consider, $N \sim O(10^4)$ typically, and direct solution schemes can be quite expensive. In the present work, we solve the BIE algebraic system using a generalized minimum residual (GMRES) algorithm (Saad & Schultz 1986) with symmetric successive over-relaxation (SSOR) pre-conditioning. The computational effort of this algorithm required for the QBEM equations is found to be at most $\sim O(N^{2.3})$ (see Xü & Yue 1992).

3.2. *Time integration*

Once the BVP at each time step is solved and the velocity $\nabla\phi$ on $\mathscr{F}$ obtained from ϕ and ϕ_n on $\mathscr{F}$, the free-surface boundary conditions (2.3) and (2.4) can be integrated in time in a straightforward manner. Here, a fourth-order Adams–Bashforth–Moulton (ABM4) integrator coupled with a fourth-order Runge–Kutta (RK4) scheme for (re)starting (whenever there is a change in time-step size) is used. ABM4 and RK4 require two and four solutions of the BVP per time step, respectively.

In the simulations, we adopt dynamic time stepping with the time-step size determined by

$$\Delta t \leqslant C_n(\Delta l)_{\min}/|(\nabla\phi)_{\mathscr{F}}|_{\max}, \qquad (3.1)$$

where $(\Delta l)_{\min}$ is the minimum distance between two neighbouring nodes on $\mathscr{F}$ and $|(\nabla\phi)_{\mathscr{F}}|_{\max}$ is the magnitude of the maximum (nodal) velocity on $\mathscr{F}$. Equation (3.1) can be derived directly from (2.3), with C_n, the Courant number, a computational parameter to be selected for stability (typically $C_n < 1$). In practice, it is useful also to impose minimum and maximum time-step limits: $\Delta t_{\min} \leqslant \Delta t \leqslant \Delta t_{\max}$.

3.3. *Removal of saw-tooth instabilities*

In the absence of numerical damping in MEL simulations, saw-tooth instabilities eventually develop on the free surface as nonlinearity increases (e.g. Longuet-Higgins & Cokelet 1976). The presence of saw-tooth instabilities can be expected in theory for a nonlinear system without dissipation, wherein energy cascades from low to high wavenumbers and accumulates at the highest wavenumber associated with the discretization. However, the appearance of saw-tooth instabilities in the simulation of breaking waves seems to depend on the BIE formulation. With the Green-theorem formulation, severe saw-tooth instabilities usually appear near the crests of steep waves, while no apparent saw-tooth instability effect is observed with the Cauchy-integral formulation (e.g. Dold 1992). The possible reason for this is that with the Green-theorem/Cauchy-integral formulation, we encounter the first/second-kind Fredholm integral equation. Usually, it is easier to obtain an accurate solution to the second-kind equation than to the first-kind equation.

| | | QBEM | | | | | CIM | | | |
| | | u | | w | | | u | | w | |
ϵ	N_w	$\bar{e}$	$e_{\max}$	$\bar{e}$	$e_{\max}$	N_w	$\bar{e}$	$e_{\max}$	$\bar{e}$	$e_{\max}$
0.2	8	0.00954	0.02169	0.00660	0.01953	32	0.00478	0.01302	0.00884	0.01801
	16	0.00099	0.00178	0.00205	0.00416	64	0.00125	0.00329	0.00225	0.00453
	32	0.00016	0.00063	0.00064	0.00170	128	0.00032	0.00082	0.00059	0.00113
	64	0.00003	0.00009	0.00017	0.00043	256	0.00008	0.00022	0.00017	0.00030
0.4	8	0.02463	0.05460	0.01165	0.02547	32	0.00388	0.03625	0.01350	0.06765
	16	0.00271	0.00914	0.00581	0.02914	64	0.00106	0.01019	0.00378	0.01942
	32	0.00027	0.00094	0.00126	0.00640	128	0.00028	0.00261	0.00101	0.00523
	64	0.00010	0.00045	0.00055	0.00238	256	0.00007	0.00065	0.00029	0.00132

TABLE 1. Normalized average ($\bar{e}$) and maximum ($e_{\max}$) errors in the horizontal (u) and vertical (w) velocities on the surface of a Stokes wave with wavenumber $k = 1$ and steepness ϵ. The three-dimensional QBEM solution uses a non-uniform grid with an average of N_w unknowns per wavelength while the CIM solution employs a uniform grid.

To remove saw-tooth instabilities, a variety of smoothing techniques can usually be used (e.g. Dommermuth *et al.* 1988; Wang, Yao & Tulin 1994). In the present simulations, we use a second-order thirteen-point Savitzky–Golay type smoothing filter (Hamming 1983) which is applied every N_s (N_s typically 3 or 6) time steps.

3.4. *Convergence tests*

The three-dimensional MEL/QBEM code has been tested extensively for accuracy and convergence. These tests include comparisons to exact (longitudinal and oblique) Stokes waves, and existing two-dimensional MEL results for overturning waves. For brevity, only representative results are given here. Extensive validation results can be found in Xü (1992) and Xue (1997).

To test the QBEM BVP solver, we input the profile and surface potential values for exact two-dimensional progressive Stokes wave (with wavenumber $k = 1$ and steepness ϵ) and solve for the surface velocity using a three-dimensional QBEM code. (For the solution of the Stokes wave, we follow Schwartz (1974) but solve the mapping by direct numerical iterations). Table 1 shows the convergence of QBEM results of the horizontal (u) and vertical (w) velocities for two wave steepness $\epsilon = 0.2$ and 0.4. For comparison, we also present results obtained by a Cauchy-theorem-based approach, which is almost identical to Vinje & Brevig (1981) but differs from Dold & Peregrine (1986) in free-surface discretization and time integration. For convenience, we hereafter denote this Cauchy integral method by CIM. The results in table 1 show that for both QBEM and CIM, the average ($\bar{e}$) and maximum ($e_{\max}$) errors in u and w decrease quadratically with increasing number of nodes (N_w) per wavelength. For a given N_w, $\bar{e}$ is much smaller than $e_{\max}$. However, for a given accuracy, CIM requires approximately four times the number of unknowns used in QBEM.

Similar convergence results are obtained when the Stokes wave is oblique to the QBEM grid. An extensive study of the evolution of such waves on varying N_w, C_n and N_s were conducted to validate the remaining part of MEL. The details of these results are omitted for brevity (see Xü 1992).

For more stringent tests, we simulate two-dimensional deep-water overturning waves using the general three-dimensional MEL/QBEM program. We use a two-dimensional Airy wave as an initial condition and compare the QBEM simulation to
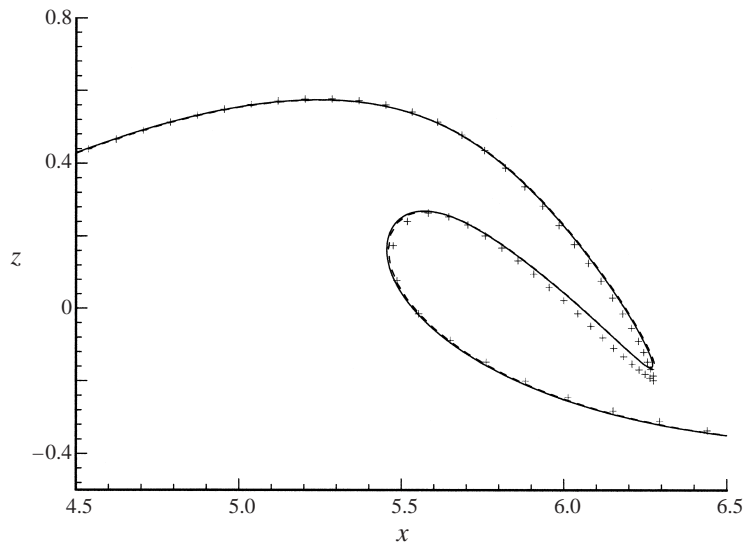
FIGURE 1. Free surface profile at $t = 4.02$ during fully nonlinear evolution of a two-dimensional Airy wave of steepness $kA = 0.544$. Plotted are the results obtained by QBEM (+); CIM (———) and D. H. Peregrine (personal communication) (- - -). The QBEM solution between two neighbouring nodes has a quadratic variation with space.

high-resolution CIM results. The initial free-surface elevation and potential are given by

$$\eta(x, t = 0) = A \cos kx, \quad \phi(x, z = \eta(x), t = 0) = A \sin kx. \quad (3.2)$$

For the simulation, we choose wavenumber $k = 1$ and amplitude $A = 0.544$. For this value of kA, the wave eventually overturns. For this two-dimensional problem, we use the three-dimensional QBEM code with one (or two) elements in the (invariant) transverse direction.

Figure 1 shows the free-surface profiles of the overturning wave near the final stage of wave breaking ($t = 4.02$) obtained using QBEM and CIM simulations. The result of D. H. Peregrine (personal communication), who used the Cauchy-integral approach of Dold & Peregrine (1986), is also shown for comparison. For the QBEM computation, we use $N_w = 96$ free-surface nodes (48 quadratic elements) per wavelength and apply a thirteen-point Savitzky–Golay-type smoothing every $N_s = 6$ time steps. The QBEM simulation conserves the (normalized) total energy to within $O(10^{-4})$. For the CIM simulation, we use $N_w = 960$, $\Delta t = 0.005$ and $N_s = 20$ (for smoothing) and obtain energy conservation to within $O(10^{-6})$. The simulation of D. H. Peregrine, who used $N_w = 192$ and no smoothing, conserves the total energy to within $O(10^{-7})$. (Note that QBEM simulations can obtain better energy conservation at higher resolution, but these simulations fail earlier due to numerical effects.) From figure 1, we see that the results of the overturning wave profile obtained using different approaches agree each other very well except in a small region near the plunging tip, where the tip by QBEM appears slightly ahead of the others.

Figure 2 plots the variation of the relative normal acceleration of the free surface (A_n) in the neighbourhood of the plunging tip well into the overturning wave development ($t = 3.41$). Here $A_n \equiv (\boldsymbol{a} - \boldsymbol{g}) \cdot \boldsymbol{n}$ where, at a given free-surface point, $\boldsymbol{a}$ is the particle acceleration, $\boldsymbol{n}$ the outward unit normal, and $\boldsymbol{g}$ the gravitational acceleration. For reference, the profile of the plunging tip is also shown. The results of A_n obtained
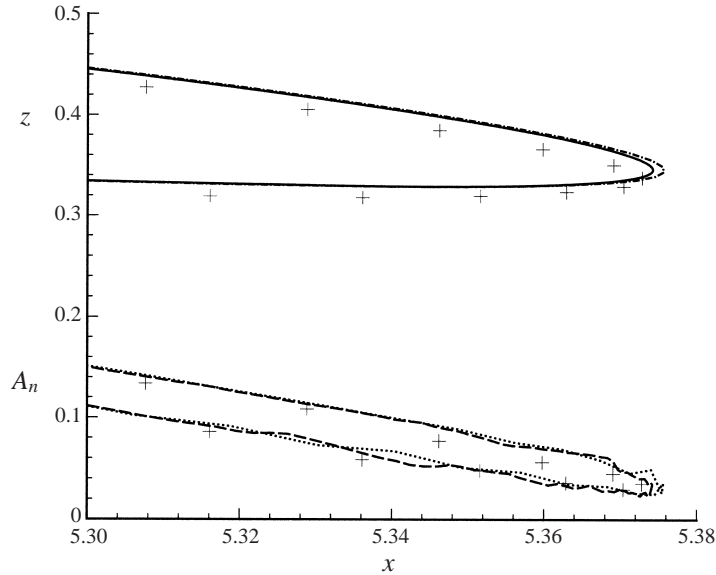
FIGURE 2. Free-surface profile $z(x)$ (upper graphs) and normal relative free-surface acceleration $A_n(x)$ (lower graphs) in the neighbourhood of the plunging tip at $t = 3.41$, during fully nonlinear evolution of a two-dimensional Airy wave of steepness $kA = 0.544$. Plotted are $z(x)$ by QBEM (+), CIM (——) and D. H. Peregrine (— · —); and $A_n(x)$ by QBEM (+), CIM (- - -) and Peregrine (1999) (· · ·). The free-surface profile above/below the plunging tip corresponds to larger/smaller A_n. (Note that the x-coordinate is stretched.)

by QBEM, CIM and D. H. Peregrine compare with each other very well. It is seen that A_n becomes smaller on moving closer to the plunging tip. All these simulations show that A_n remains positive in the plunging tip region and approaches zero during the final stage of overturning wave development.

The above convergence tests and comparisons to high-resolution computations of two-dimensional overturning waves provide the guidelines for the choice of computational parameters for our subsequent QBEM studies of three-dimensional steep/breaking waves.

4. Dynamics of three-dimensional breaking waves

As a first application, we apply our method to study the dynamics of three-dimensional overturning waves. Our main objective is to quantify the three-dimensional kinematics of such waves and the dynamics leading to wave breaking in three dimensions.

4.1. *Kinematics of three-dimensional overturning waves*

We extend the two-dimensional MEL results of Longuet-Higgins & Cokelet (1976) for overturning waves to three dimensions. Following their work, we start with a plane Stokes wave but now apply, for a short time, a three-dimensional surface pressure to raise the energy density beyond the maximum for a steady (two-dimensional) Stokes wave.

As initial conditions, we choose the Stokes wave parameters: wavelength $L = 2\pi$, steepness $\epsilon = 0.4$, period $T \cong 5.806$ and phase speed $c \cong 1.082$. The imposed surface pressure has the same temporal (t) and longitudinal (x) dependence as in the fourth
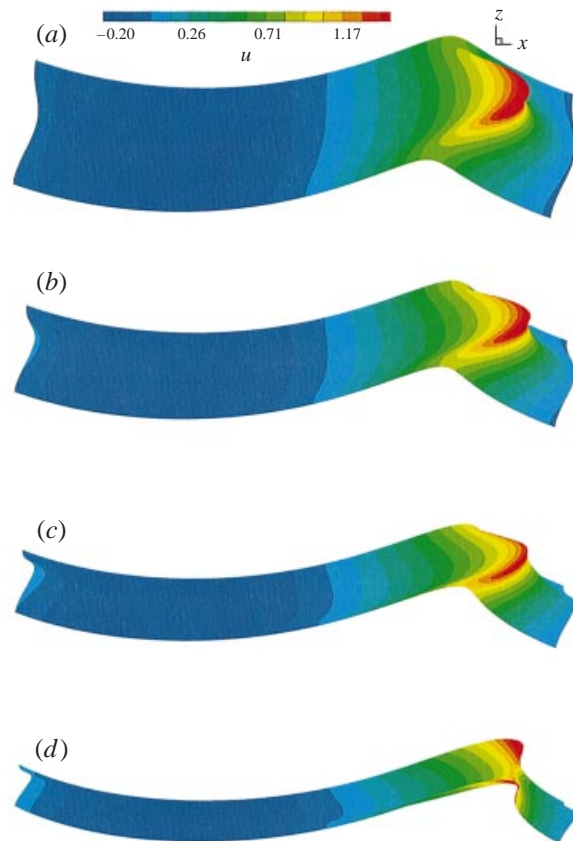
FIGURE 3. Distributions of the surface longitudinal velocity u at the late stage of three-dimensional overturning waves for different values of γ : (*a*) 1.5 (at $t/T = 0.840$); (*b*) 1.0 ($t/T = 0.850$); (*c*) 0.75 ($t/T = 0.861$); and (*d*) 0.5 ($t/T = 0.880$). (The phase speed of the initial Stokes wave $c = 1.082$.)
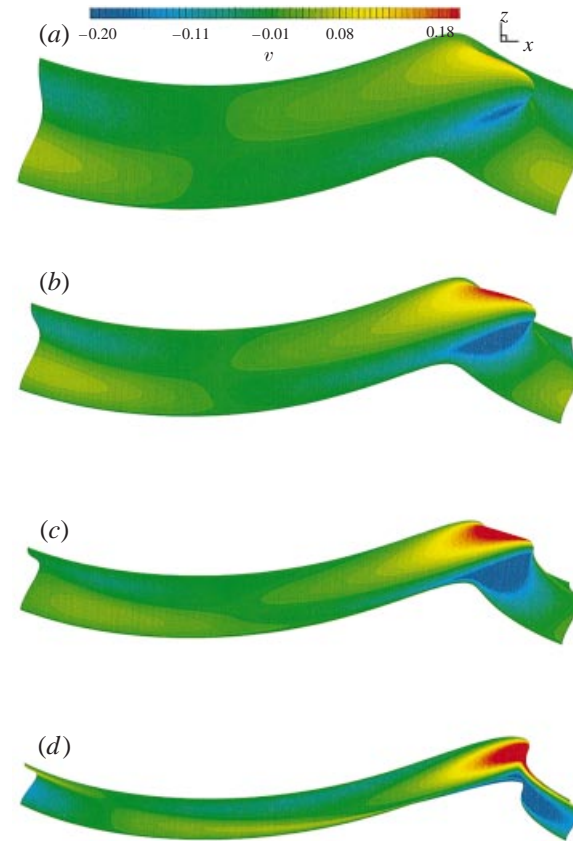
FIGURE 4. Distributions of the surface transverse velocity v at the late stage of three-dimensional overturning waves for different values of γ : (*a*) 1.5 (at $t/T = 0.840$); (*b*) 1.0 ($t/T = 0.850$); (*c*) 0.75 ($t/T = 0.861$); and (*d*) 0.5 ($t/T = 0.880$). (The phase speed of the initial Stokes wave $c = 1.082$.)

Three-dimensional wave–wave and wave–body interactions. Part 1

21

case studied by Longuet-Higgins & Cokelet (1976), but is now further modulated by a periodic transverse variation of wavelength W:

$$P_{\mathscr{F}} = \begin{cases} p_0 \cos^2(\pi y/W) \sin t \sin(x - ct), & 0 \leqslant t \leqslant \pi \\ 0, & t > \pi, \end{cases} \tag{4.1}$$

where $p_0 = 0.146$. The co-propagating surface pressure increases from 0 at $t = 0$ to its maximum amplitude at $t = \pi/2$ ($t/T \cong 0.271$) and decreases to zero for $t \geqslant \pi$. Note that (4.1) is symmetric with respect to $y = 0$ and $\pm W/2$, so that the unknowns in the double-periodic domain of L by W can be halved by taking advantage of symmetry. Physically, the problem can be thought of as one in a wave tank with sidewalls at any two values of $mW/2$, $m = 0, \pm 1, \pm 2, \dots$. For definiteness, we refer hereafter to $y = 0$ where $P_{\mathscr{F}} = p_0$ is maximum as the 'centre', and $y = \pm W/2$ where $P_{\mathscr{F}} = 0$ is minimum as the 'sides'.

The geometric aspect ratio $\gamma \equiv W/L$ provides a measure of the three-dimensionality of the wave. To illustrate the importance of the three-dimensional effect and the difference from two-dimensional results, we perform systematic simulations for a range of $\gamma = 0.5, 0.75, 1.0, 1.25$, and 1.5. Based on convergence tests, we employ 65×25 free-surface grids (384 9-node quadratic elements) corresponding to $N = 1600$ unknowns for half of the computational domain, $[0, L] \times [-W/2, 0]$. The Courant number is set to be $C_n = 0.6$ for $t \leqslant \pi$ and $C_n = 0.4$ for $t > \pi$. Thirteen-point Savitzky–Golay-type smoothing is applied every $N_s = 3$ time steps. The initial free-surface Lagrangian points are distributed non-uniformly according to the curvature of the Stokes waves and are followed throughout the simulation without regridding. The energy loss due to smoothing is less than 0.01% for the entire simulation. The simulation (with $N = 1600$) uses $O(5)$ minutes (single processor) CPU time on a CRAY-YMP supercomputer for each time step.

Figures 3, 4, and 5 show the free-surface profiles and particle velocity components u, v, w, near the final stages of the three-dimensional overturning waves, for $\gamma = 1.5, 1.0$, 0.75 and 0.5. The free-surface profile, u and w are symmetric while v is antisymmetric about the centreline $y = 0$. The results for different values of γ can be qualitatively quite different. In particular, the three-dimensional wave plunging occurs near the centre (where the pressure forcing was maximum) for $\gamma = 1.5$ and 1.0; for $\gamma = 0.5$, the plunging wave develops near the side (where the forcing was minimum). For $\gamma = 0.75$, the plunging tip is located between the centre and the side of the tank.

This seemingly surprising result can be explained heuristically by a qualitative consideration of the period of transverse wave sloshing in the 'tank'. According to linear theory, the sloshing period of the first-mode transverse wave is given by

$$T_W/T_L = [1 + \gamma^{-2}]^{-1/4}, \tag{4.2}$$

where $T_L(= 2\pi$ here) is the linear longitudinal period. This corresponds to $T_W/T_L \simeq 0.912, 0.841, 0.775, 0.669$ for $\gamma = 1.5, 1.0, 0.75, 0.5$ respectively. Assuming that a transverse wave in phase with (4.1) is established when the applied pressure is removed (at $t_1 = \pi$), the sloshing wave will reach a maximum amplitude at the sidewalls at $t_2 \simeq t_1 + T_W/2 = 1.035T, 0.997T, 0.961T, 0.903T$ for $\gamma = 1.5, 1.0$, $0.75, 0.5$, respectively. For $\gamma = 1.5, 1.0$ and 0.75, the computed plunging times (which depend in general on the energy input and the nonlinear dynamics) are at $t/T = 0.84$, 0.85 and 0.86, which are appreciably less than t_2. For $\gamma = 0.5$, however, this plunging time is $t/T = 0.88$, which is close to the arrival of the cross-mode crest at the sidewall. Thus, the plunging locations in figures 3–5 can be qualitatively explained. Since the breaking location depends in general on the balance between the transverse dynamics

and the nonlinear development of the plunging wave, an important consequence is that three-dimensional breakers need not develop directly behind the region of maximum (surface or bottom) forcing.

The sequence of development in time of the plunging wave profiles and surface velocity components u, v, w is shown in figure 6 for $\gamma = 1.5$. When the surface forcing is turned off at $t = \pi$, the deviation from the two-dimensional Stokes wave is relatively small, although three-dimensional features of this 'initial' condition are evident. As the wave steepens and the free surface eventually plunges forward and overturns, the horizontal velocity u on the centreline increases to almost three times its initial value. In contrast, changes in the magnitudes of the maximum and minimum vertical velocity w as the plunging wave develops are insignificant. Overall, the ratio of maximum u to maximum w, $(u/w)_m$, increases from an initial value of 1.4 to 3.5 as the wave overturns. Thus, wave overturning is primarily a result of the longitudinal motion.

The relatively short time to breaking (relative to transverse oscillation period) in this case does not allow significant energy transfer from the centre to the sides. This is seen in figure 6 for the surface v. By virtue of symmetry, v vanishes at $y = 0, \pm W/2$, and is only non-zero in between. This transverse velocity is positive (towards the plunger at the centreline) on the front face, and negative near and behind the wave crest. At the final time instant shown, the ratio of maximum u to v for this value of $\gamma = 1.5$ is $(u/v)_m = 20.1$ and the overall effect of the transverse velocity is small.

Finally, we plot in figure 7 representative surface streamlines at the late stage of wave plunging ($t/T = 0.85$) for the case $\gamma = 1.0$. Here the longitudinal velocity is defined relative to the phase velocity of the initial Stokes wave ($c = 1.082$). The contour of v on the wave surface is also shown. In the region of wave overturning, there is a strong transverse flow toward the side ($y = -W/2$) while the plunging tip, which is (nearly) the highest point of the wave, is near the centre ($y = 0$). Note that the longitudinal velocity (u) exceeds the wave phase speed c near the plunging tip (for clarity, the streamlines are omitted in a small region near the tip).

4.2. *The effect of three-dimensionality*

In this section, we address the effect of three-dimensionality. Our interest is to obtain direct comparisons of wave characteristics such as profiles, velocities and accelerations, and kinetic and potential energies, for plunging waves with different three-dimensionality parameter γ. To do this, it is useful to define a reference time t^* at which such comparisons can be made. One choice is $t^* = t_v$, the instant at which the free surface first becomes vertical. In these simulations, however, t_v occurs at a relatively early stage of the plunging wave development. For $t > t_v$, the plunging wave kinematics continues to change rapidly. A more useful choice is to define t^* to be the instant at which the condition of free fall ($A_n \approx 0$) at the plunging tip first obtains. (For definiteness, we define t^* to be given by $(A_n)_{\min}(t^*) = 0.02$, say, where $(A_n)_{\min}$ is the minimum value of A_n on the entire free surface.) At the tip region for $t \approx t^*$, the longitudinal velocity has effectively reached its maximum value, while the (subsequent) vertical velocity is predictable given essentially by the condition of free fall. While this choice of t^* is by no means unique, it is a pragmatic one since it is a late time we can (quantitatively) identify beyond which the good fidelity of our numerical simulation cannot be guaranteed.

Table 2 gives the time t^*, and the plunging tip position and velocity at that instant for three-dimensional overturning waves with a range of the three-dimensionality parameter γ. Here the tip is defined to be the point where $A_n = (A_n)_{\min} = 0.02$ at
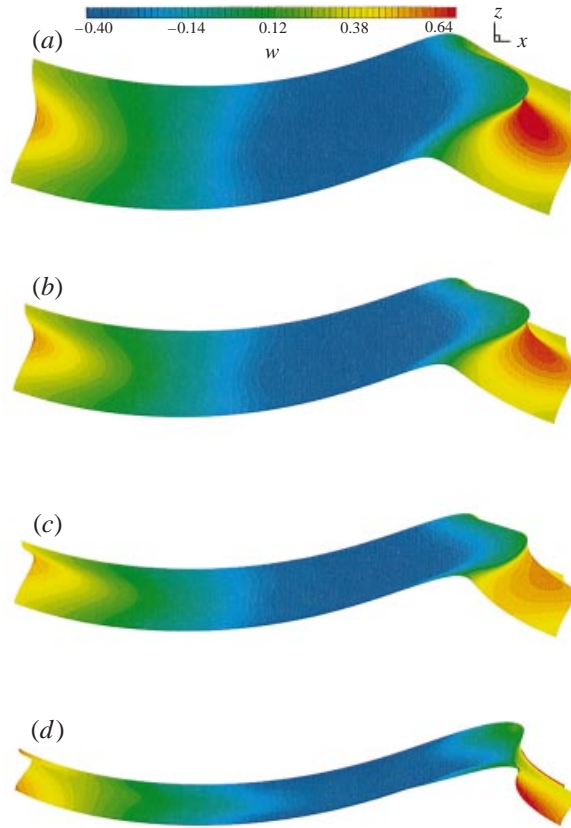
FIGURE 5. Distributions of the surface vertical velocity w at the late stage of three-dimensional overturning waves for different values of γ : (*a*) 1.5 (at $t/T = 0.840$); (*b*) 1.0 ($t/T = 0.850$); (*c*) 0.75 ($t/T = 0.861$); and (*d*) 0.5 ($t/T = 0.880$). (The phase speed of the initial Stokes wave $c = 1.082$.)
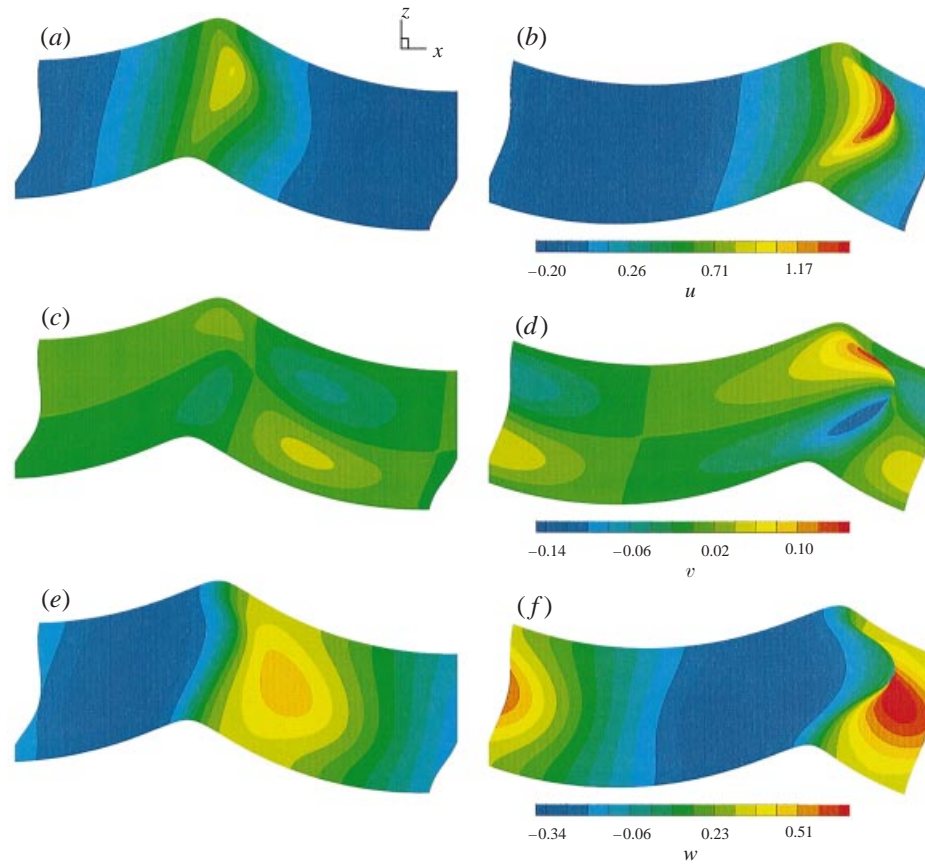
FIGURE 6. Distributions of the surface velocity components u, v and w for $\gamma = 1.5$. The results plotted are for u at (*a*) $t/T = 0.541$ and (*b*) 0.840; for v at (*c*) $t/T = 0.541$ and (*d*) 0.840; and for w at (*e*) $t/T = 0.541$ and (*f*) 0.840. (The phase speed of the initial Stokes wave $c = 1.082$.)

γ	0.50	0.75	1.00	1.25	1.50	∞
t^*/T	0.879	0.861	0.849	0.842	0.839	0.813
X_{tip}	6.234	6.313	6.328	6.316	6.313	6.080
Y_{tip}	−1.312	0.000	0.000	0.000	0.000	0.000
Z_{tip}	0.695	0.755	0.749	0.725	0.707	0.660
$|V_{\text{tip}}|$	1.665	1.487	1.618	1.708	1.751	1.771
u_{tip}	1.633	1.474	1.613	1.706	1.751	1.771
v_{tip}	−0.304	0.000	0.000	0.000	0.000	0.000
w_{tip}	0.112	0.180	0.115	0.060	0.005	−0.035

TABLE 2. Time t^* (normalized by the fundamental period of the initial Stokes wave $T = 5.806$), and the tip position (X_{tip}, Y_{tip}, Z_{tip}), amplitude of the tip velocity V_{tip} and its three components (u_{tip}, v_{tip}, w_{tip}), at $t = t^*$, of overturning waves for a wide range of γ values.
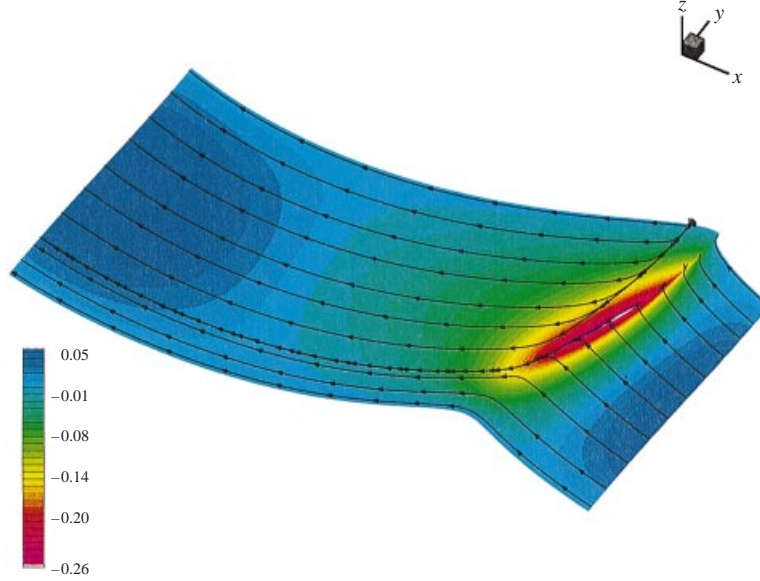

FIGURE 7. Surface transverse velocity (v) contours and surface streamlines with velocity relative to the phase velocity of the initial Stokes wave ($c = 1.082$). The results plotted (for $y = [0, -W/2]$) are for $\gamma = 1.0$ at $t/T = 0.85$.

$t = t^*$. For comparison, the corresponding values for a two-dimensional overturning wave (corresponding to $\gamma = \infty$) are also given. It is observed that t^* for the three-dimensional wave is always larger than that for the two-dimensional wave, and that t^* decreases uniformly as γ increases. This confirms the general expectation that breaking of a three-dimensional wave would take longer to develop.

As a result of the larger t^*, X_{tip} and Z_{tip} are generally greater for the three-dimensional overturning wave than in the two-dimensional case. For small γ (< 0.75), X_{tip} and Z_{tip} increase with γ while Y_{tip} is negative as a result of shift of wave breaking from the centre to the side. Beyond this value of γ, X_{tip}, Z_{tip} approach the two-dimensional values monotonically as γ increases, while $Y_{\text{tip}} = 0$ (wave breaking at the centre).

γ	0.50	0.75	1.00	1.25	1.50	∞
V_{max}	1.885	1.536	1.748	1.859	1.921	1.846
$(V_x)_{max}$	1.875	1.500	1.742	1.859	1.920	1.831
$(V_y)_{max}$	0.056	0.043	0.056	0.059	0.056	0.000
$(V_z)_{max}$	0.748	0.591	0.678	0.710	0.721	0.692
V_{min}	0.260	0.268	0.255	0.249	0.246	0.327
$(V_x)_{min}$	−0.295	−0.305	−0.321	−0.328	−0.331	−0.336
$(V_y)_{min}$	−0.321	−0.371	−0.268	−0.199	−0.160	0.000
$(V_z)_{min}$	−0.453	−0.398	−0.410	−0.413	−0.413	−0.428
A_{max}	3.587	2.552	3.210	4.102	5.073	3.988
$(A_x)_{max}$	3.224	2.201	2.720	3.119	3.368	3.682
$(A_y)_{max}$	0.383	0.128	0.079	0.060	0.049	0.000
$(A_z)_{max}$	0.511	0.386	0.406	0.427	0.442	0.494
A_{min}	0.089	0.063	0.085	0.057	0.044	0.247
$(A_x)_{min}$	−0.425	−0.402	−0.388	−0.388	−0.392	−0.365
$(A_y)_{min}$	−0.252	−0.750	−0.667	−0.573	−0.506	0.000
$(A_z)_{min}$	−2.224	−1.873	−2.571	−3.861	−4.934	−2.941
η_{max}	0.811	0.761	0.758	0.746	0.735	0.696
η_{min}	−0.266	−0.259	−0.263	−0.266	−0.269	−0.286
$\eta_{max} - \eta_{min}$	1.077	1.020	1.021	1.011	1.004	0.983

TABLE 3. Maximum $(( )_{max})$ and minimum $(( )_{min})$ values on the free surface of the velocity amplitude, V, and velocity components, V_x, V_y, V_z; acceleration amplitude, A, and acceleration components, A_x, A_y, A_z; and wave elevation, η, at $t = t^*$, of overturning waves for a wide range of γ values.

The tip velocity amplitude $|V_{tip}|$ is generally smaller than the two-dimensional value. $|V_{tip}|$ generally increases with γ except for very small γ where the transverse sloshing can significantly increase the magnitude of the tip velocity. The behaviour of V_{tip} is dominated by its longitudinal component u_{tip} which is an order of magnitude larger than the transverse and vertical velocities v_{tip} and w_{tip}. For three-dimensional plunging waves, w_{tip} is positive and decreases monotonically with increasing γ for $\gamma > 0.75$. On the other hand, w_{tip} is negative for the two-dimensional case. This is consistent with the larger value of Z_{tip} for the three-dimensional case. The transverse tip velocity v_{tip} for the three-dimensional wave is generally negligible except for the case of small γ where it is negative as a result of the shift of the plunging tip from the centre to the side. (Note that for the case $\gamma = 0.50$, $v_{tip} \neq 0$ since the tip is close to, but not exactly on, the side.)

Table 3 displays the maximum and minimum values of the velocity and acceleration amplitudes and components on the free surface at the time t^*. Note that the plunging wave V_{max} is substantially greater than the phase speed of the initial Stokes wave ($c \cong 1.082$). V_{max} usually occurs at a point near the tip but not at the tip. Compared to V_{tip}, V_{max} is about 10% larger. From the simulations, V_{max} is achieved at the centre for $\gamma \geqslant 1.0$ and on the side for $\gamma = 0.5$. For $\gamma = 0.75$, which is a transitional case, V_{max} occurs between the centre and the side. Unlike V_{tip}, V_{max} of the three-dimensional wave can be greater than that of the two-dimensional wave. Similarly to u_{tip}, $(V_x)_{max}$ is much larger than $(V_y)_{max}$ and $(V_z)_{max}$ and behaves similarly to V_{max}. Due to the effect of transverse sloshing, $(V_z)_{max}$ varies inversely with $|(V_y)_{min}|$. Thus there is a strong energy and momentum transfer from the vertical to transverse motion in the development of the three-dimensional overturning waves.
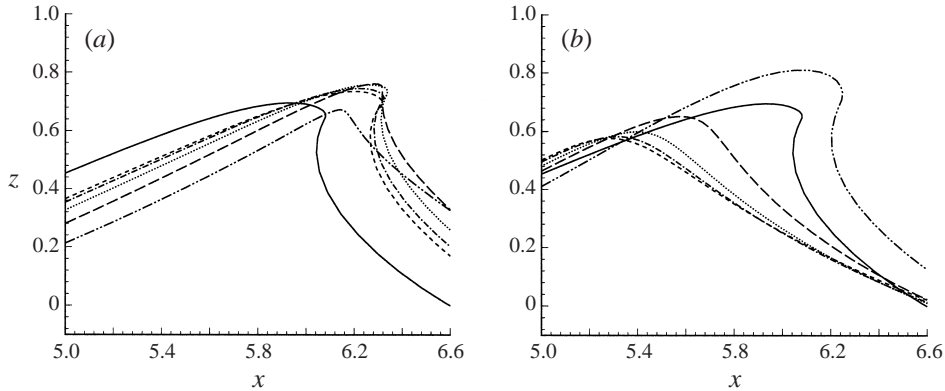
FIGURE 8. Free-surface profiles of two- and three-dimensional overturning waves at the time t^* on (a) the centre-plane; and (b) the side for: $\gamma = \infty$ (——); $\gamma = 1.5$ (- - -); $\gamma = 1.25$ (— · —); $\gamma = 1.0$ (· · ·); $\gamma = 0.75$ (– – –); and $\gamma = 0.5$ (— · · —).

The variation of the maximum free-surface acceleration magnitude $A_{\max}$ with γ is similar to that of $V_{\max}$. $A_{\max}$ usually occurs under the tip at the front face of the overturning wave and reaches values of $O(5g)$. $A_{\max}$ of the three-dimensional overturning wave can be larger or smaller than the two-dimensional result, depending on γ. Specifically, for $\gamma > / < 1.25$, $A_{\max}$ is greater/smaller than that of the two-dimensional value. This behaviour of $A_{\max}$ is seen to be strongly correlated with the magnitude of $(A_z)_{\min}$. For longitudinal free-surface acceleration, $(A_x)_{\max}$ is generally smaller in the presence of three-dimensionality. In the transverse direction, there is appreciable A_y primarily associated with the sloshing motion towards the side (as reflected in larger $|(A_y)_{\min}|$ values).

The dependence on γ of the maximum and minimum wave elevations $\eta_{\max}$, $\eta_{\min}$ and wave height $h \equiv \eta_{\max} - \eta_{\min}$ at t^* is also shown in table 3. In general, h and $\eta_{\max}$ of the three-dimensional overturning wave exceed those of the two-dimensional case. Both h and $\eta_{\max}$ are seen to decrease uniformly as γ increases. For small γ, the three-dimensional h can be about 15% larger than the two-dimensional value. For $\eta_{\min}$, there is no significant difference between the two-dimensional and three-dimensional cases.

The free-surface profiles of the overturning wave on the centre- and side-planes at the time t^* are shown in figure 8 for different γ. Except for $\gamma = 0.5$ where wave breaking occurs near the side, three-dimensional waves break with higher tip/crest at the centre-plane than the two-dimensional wave. Careful examination of the centre-plane profiles reveals that the $\gamma = 1.25$ case has a profile shape most similar to the two-dimensional plunging wave. For $\gamma < / > 1.25$, the overturning waves have less/more arced (concaved) front faces than for the two-dimensional case.

Two main factors affect the development of the overturning profile. One is the nonlinear free-surface focusing from both the longitudinal and transverse directions. This explains why the three-dimensional wave can be more energetic on the centre-plane. The other is transverse sloshing which spreads the energy from the centre-plane to the side. For $\gamma < / > 1.25$, the second/first factor dominates resulting in less/more forward-face concaved centre-plane profiles.

The sidewall profiles (figure 8b) show the wave breaking there of the $\gamma = 0.5$ case. The concentration of energy here results in much higher crest/tip than the
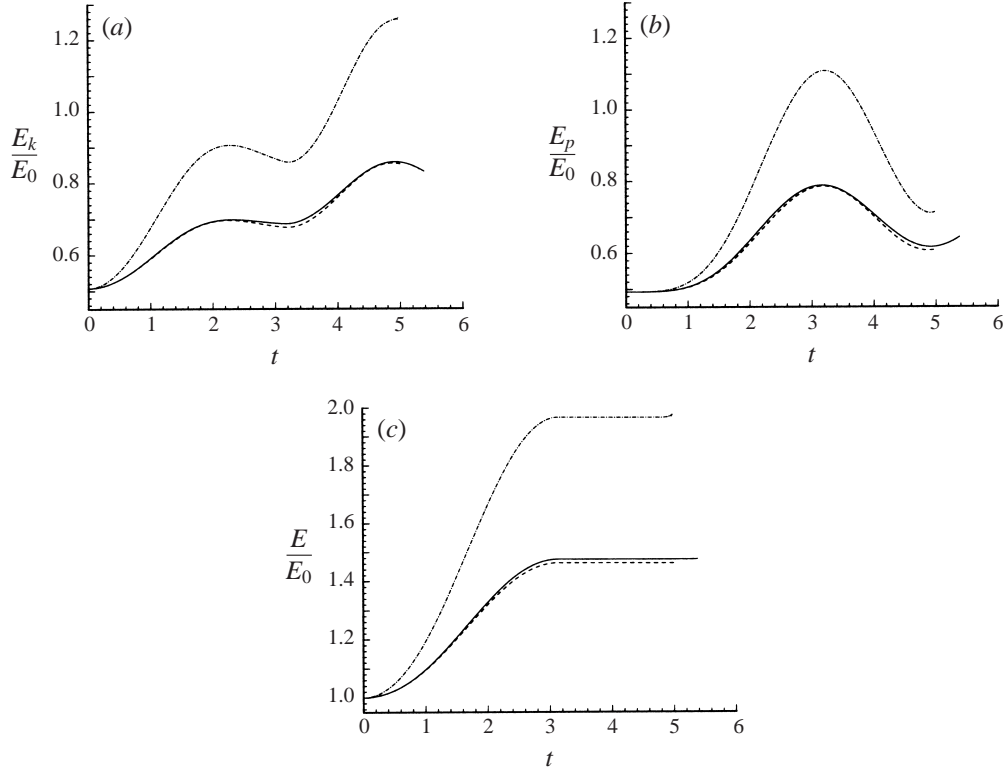
FIGURE 9. Time histories of (*a*) kinetic energy E_k, (*b*) potential energy E_p, and (*c*) total energy $E \equiv E_k + E_p$, normalized by the total energy of the initial Stokes wave E_0, for: $\gamma = \infty$ (— · —); $\gamma = 1.5$ (- - -); and $\gamma = 0.5$ (——).

two-dimensional overturning wave. The large t^* also results in a more forward profile position. For larger γ (> 0.5), the sidewall profiles are lower and non-breaking.

Figure 9 shows the evolution of the kinetic energy E_k, potential energy E_p and total energy $E \equiv E_k + E_p$ (in the entire computational domain), normalized by the total energy of the initial Stokes wave E_0, for $\gamma = \infty$, 1.5, and 0.5. The other γ cases are considered but not shown here for clarity as results are similar. With the surface pressure forcing given by (4.1), E_k and E_p in the three-dimensional case are only weakly dependent on γ. Due to transverse modulation in (4.1), these values are, as expected, smaller than those of the two-dimensional wave ($\gamma = \infty$). At the initial stage, under the imposition of the free-surface pressure, E_k, E_p and E increase with time. At $t \cong 3.14$, the pressure forcing is removed, and both E_p and E reach their maxima. Beyond this time, E remains constant while E_p decreases as E_k grows until the final stage of wave breaking.

The role of wave energy in the development of wave overturning can be better understood by examining the ratio between the kinetic-energy increase ΔE_k and the potential-energy increase ΔE_p (from the initial time). Figure 10 plots the results at the time t^* as a function of γ. It is seen that $\Delta E_k / \Delta E_p$ of the three-dimensional overturning wave is smaller than the two-dimensional result with $\Delta E_k / \Delta E_p$ increasing with γ and approaching the two-dimensional value for large γ. Thus the three-dimensional wave breaks with a larger potential energy increase but is less kinetically energetic relative to the two-dimensional case. This is consistent with earlier results that the three-
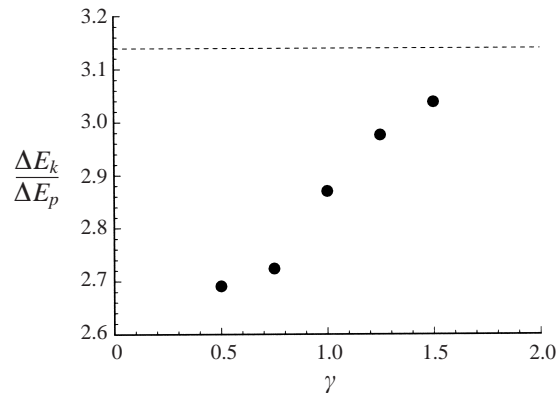
FIGURE 10. Ratio between the increases in the kinetic and potential energies ΔE_k and ΔE_p at the instant t^* of the three-dimensional overturning wave as a function of γ. The two-dimensional result is also plotted (- - -).

dimensional breaking wave has larger wave height but smaller tip velocity than the two-dimensional wave.

We remark that the above characteristics of three-dimensional overturning waves are obtained for a particular class of such waves, namely those obtained with a short-duration artificial surface pressure forcing specified by a three-dimensional parameter γ. Our choice of this scenario is motivated by the seminal work of Longuet-Higgins & Cokelet (1976) for the two-dimensional plunging wave. The features and conclusions we find can also be obtained for deep-water overturning waves generated via other mechanisms. One such mechanism is the steepening to breaking of a (transversely modulated) large-amplitude wave given initially by (linear) Airy theory (e.g. Schultz *et al.* 1994). The similarity of the overall features are confirmed by our systematic simulations also of that case (see Xue 1997, for details). The results are indeed quite similar and are not repeated in this paper.

5. Crescent waves

In this section, we investigate the mechanism for the generation and development of three-dimensional steep crescent waves (also called 'horseshoe' waves) observed in wave basins and open ocean (e.g. Su *et al.* 1982; Kinsman 1984). Postulating that such waves are the direct result of nonlinear three-dimensional wave interactions, we study the fully nonlinear evolution of large-amplitude plane Stokes wave subject to small initial three-dimensional perturbations. Specifically, we consider three-dimensional perturbations obtained from linear instability analysis of plane Stokes waves (McLean 1982), in particular, the (most) unstable class II (three-dimensional) mode(s). We perform systematic simulations to obtain the long-time three-dimensional fully nonlinear development of such a wave train. We find that steep crescent waves, similar to those observed in experiments, arise naturally from such nonlinear evolutions. Specifically we find both L_2 and L_3 crescent waves which compare quantitatively well with the experimental measurements of Su *et al.* (1982). This is contrary to Shrira *et al.* (1996), who suggest that the inclusion of non-conservative effects is necessary for the development of such waves.

We start the simulations with a train of exact plane Stokes wave (Schwartz 1974), propagating in the $+x$-direction, with fundamental wavelength $L = 2\pi/k$, steepness

kA, and phase such that the maximum elevation is at $x = 0$ at $t = 0$. We then consider initial three-dimensional perturbations to the free-surface elevation and velocity potential (η' and ϕ') given by a single sinusoidal wave component:

$$\eta' = \epsilon A \sin(k_x x + \beta) \cos k_y y, \tag{5.1}$$

$$\phi' = -\frac{\epsilon A}{(k_x^2 + k_y^2)^{1/4}} \cos(k_x x + \beta) \cos k_y y \exp[(k_x^2 + k_y^2)^{1/2} z] \quad \text{on} \quad z = \bar{\eta}, \tag{5.2}$$

where ϵ is the small parameter measuring the amplitude of the disturbance and $\bar{\eta}$ is the free-surface elevation of the undisturbed Stokes wave. Here the wavenumbers $(k_x, k_y) = (p + k, q)$, where p and q are the longitudinal and transverse perturbation wavenumbers (cf. McLean 1982). In the above, β is the phase of the perturbation which we vary in later simulations.

We set $k = 1$ for the Stokes wave. For computations, we use a rectangular domain given by $x \in [0, L/p]$ and $y \in [-L/(2|q|), 0]$ (due to transverse symmetry of the problem, only half of the y domain is needed). Based on earlier convergence tests and the required resolution for the crescent wave features, we employ 40 nodes (corresponding to 20 quadratic elements) per wavelength in both longitudinal and transverse directions. For time integration, dynamic stepping with Courant number $C_n = 0.4$ is used. With these numerical parameters, the total energy is conserved to $O(0.01\%)$ in the simulations.

5.1. *Development of L_2 crescent waves*

To simulate a L_2 crescent wave case, we choose $kA = 0.33$ (for this steepness, the fundamental period is $T \cong 5.951$) for the Stokes wave; and $\epsilon = 0.16$, $(k_x, k_y) = (1.5, 1.23)$ ($k_x = 1.5$ corresponds to $p = 1/2$), and $\beta = 0$ for the initial three-dimensional perturbation. According to McLean (1982), the latter corresponds to the dominant component of the most unstable ($p = 1/2$ sub-harmonic class II) mode for this kA.

Figure 11 shows a representative sequence of free-surface profiles during the non-linear evolution. Figure 11(*a*) shows the initial perturbed Stokes wave profile. With $\beta = 0$, the elevation perturbation is zero at the crests but is discernible (though very small) elsewhere. As will be shown later, the choice of β does not affect the overall development of the L_2 crescent wave. At $t \sim T/2$, figure 11(*b*), clear three-dimensional wave features have developed. At this stage, the largest wave slope occurs on the back faces of the Stokes wave.

At $t \sim T$, figure 11(*c*), a distinct crescent shape of the waves can be observed. Along the Stokes wave crest line, forward fronts of the crescents have sharper crest angles than the edges (where two crescents meet). Even at this early stage, the staggered row-shift crescent pattern has already been formed. As the evolution continues, the crescent shape becomes more rounded. Interestingly, the crescent pattern is seen to weaken a bit at $t \sim 2T$, figure 11(*d*).

At $t \sim 3T$, figure 11(*e*), the crescent wave development regains strength: the trough now becomes deeper, and the crest becomes sharper. Meanwhile, the edges of the crescent lines are seen to extend further in the $-x$-direction. At $t \sim 4T$, the development appears to reach a quasi-steady state. This steady state lasts for about two periods (cf. figure 11*f*, *g* at $t/T \approx 4.3$, 5.0 respectively). At this state, the sharp-crested round semi-circular and staggered row-shifted crescent crests are well-formed.

As the evolution continues further, the quasi-steady state of $t/T \sim 5$ with the
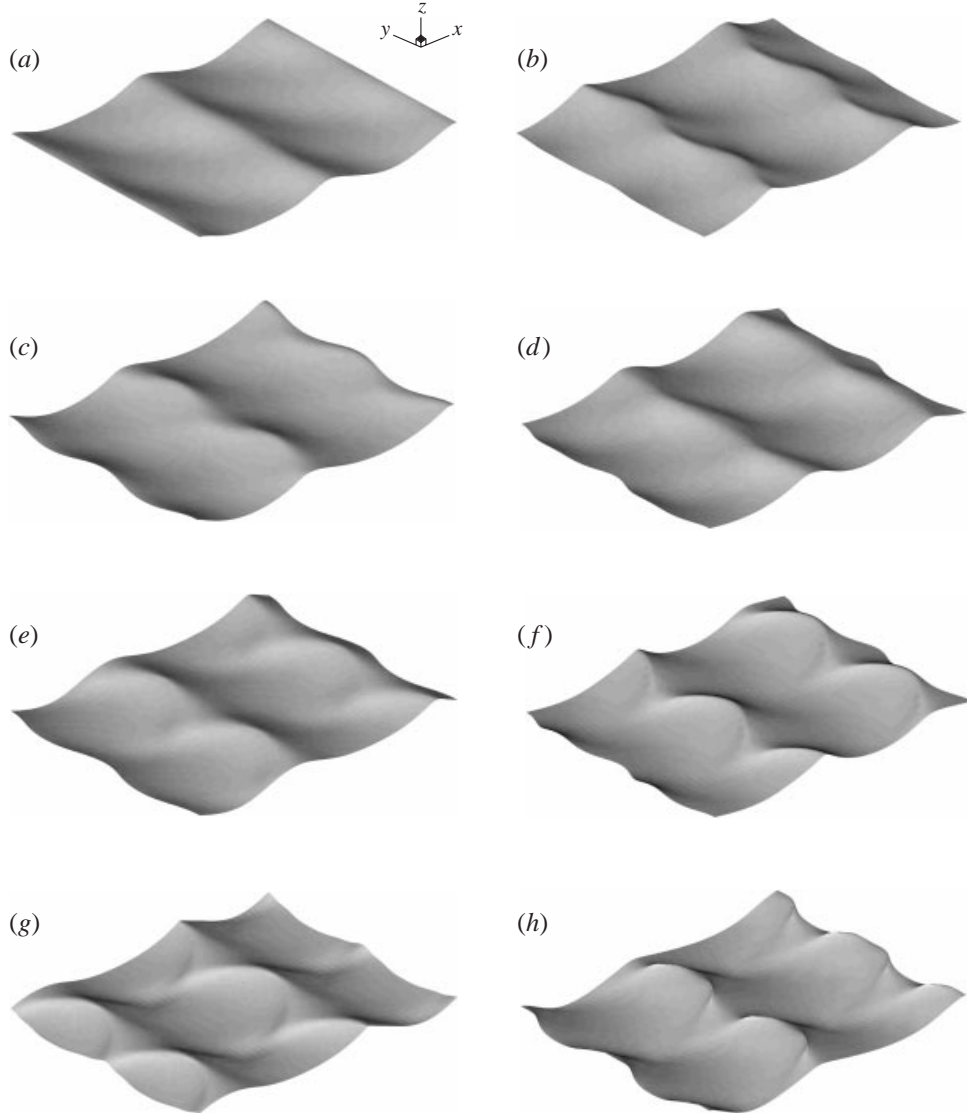
FIGURE 11. Free-surface patterns during the nonlinear evolution of a plane Stokes wave of steepness $kA = 0.33$ (fundamental period $T = 5.951$), with three-dimensional initial disturbance given by $\epsilon = 0.16$, $(k_x, k_y) = (1.5, 1.23)$ and $\beta = 0$ at (a) time $t/T = 0$; (b) 0.635; (c) 1.078; (d) 2.002; (e) 3.172; (f) 4.338; (g) 4.955; and (h) 5.641.

rounded crescent wave pattern is lost. The crescent crest sharpness is diminished and the deep trough regions flatten up. Meanwhile, steep triangular 'Delta' (Δ) regions appear in front of the crescent forward fronts. The flattening of the trough and rising of the Delta region eventually cause the crescent crests to break in the form of spilling waves on the shoulders of the crescent wave. Figure 11(h) shows a typical L_2 crescent wave pattern just before breaking.

To show the Delta region and the steep/breaking crescent wave shoulder more clearly, figure 12 plots the contours of the free-surface elevation at the same instant as figure 11(h). The distinct features of flattened troughs, steep shoulders, and steep Delta regions in front of the crescent crests are clearly shown.
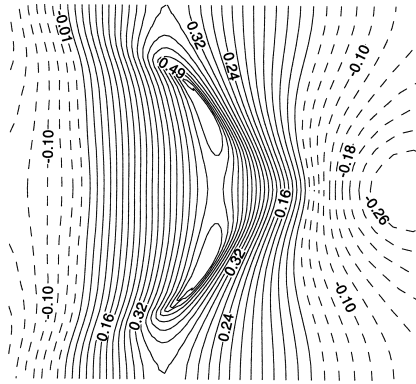
FIGURE 12. Free-surface elevation contours of the crescent wave in figure 11(*h*) (*t*/*T* = 5.641).
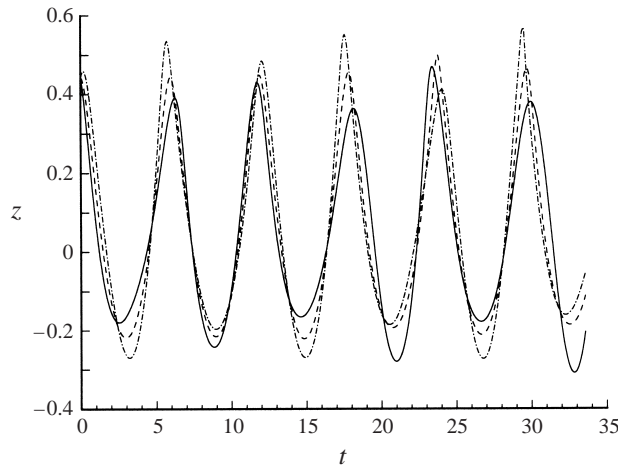

FIGURE 13. Time histories of the free-surface elevations along the line $x = 0$ with $y = y_1$ (— · —); y_2 (- - -); and y_3 (——) obtained from simulation ($kA = 0.33$, $\epsilon = 0.16$, $\beta = 0$, and $(k_x, k_y) = (1.5, 1.23)$).

The nonlinear three-dimensional evolution leading to the L_2 crescent wave de-velopment can be seen more quantitatively from time histories of the η at given x position (say the Stokes wave crest $x = 0$) and different transverse locations. Figure 13 plots $\eta(x = 0, y_i, t)$ at $2y_j q/L = -1$, -0.5, 0, for $j = 1, 2, 3$, correspond-ing respectively to the edge, shoulder and forward front of the ($x \approx 0$) crescent wave crest. The evolutions $\eta(x = 0, y_1, t)$ and $\eta(x = 0, y_3, t)$ both display alternating variations in time in amplitude and period. For each profile, the greater amplitude is associated with the smaller period and vice versa. This type of anti-correlation between the amplitude and period is a direct result of nonlinear wave dispersion. Comparing the y_1 and y_3 profiles, the greater amplitude/period in one coincides with the smaller amplitude/period in the other, which is consistent with the staggered row-shifted crescent crest feature. The $\eta(x = 0, y_2, t)$ evolution has nearly constant period and amplitude and is qualitatively similar to that of the plane Stokes wave itself.

It is useful to obtain a measure of the growth rate of the initial three-dimensional perturbation leading to the development of the crescent waves. Following Longuet-Higgins & Cokelet (1978), we define a root-mean-square growth rate $R(t)$ for the
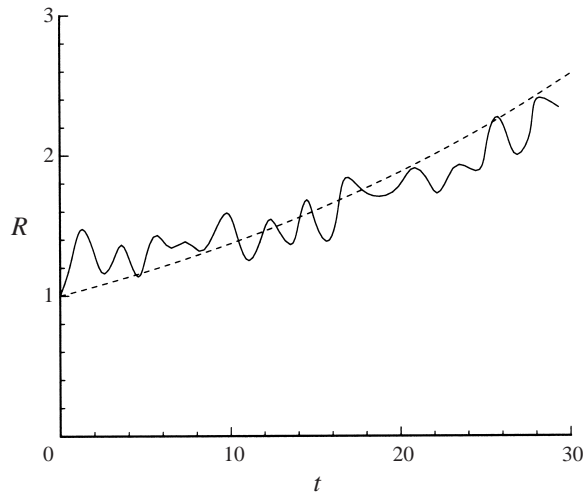
FIGURE 14. Growth rate $R(t)$ of the initial disturbance in the evolution of a perturbed Stokes wave ($kA = 0.33$, $\epsilon = 0.16$, $\beta = 0$, and $(k_x, k_y) = (1.5, 1.23)$) from fully nonlinear simulation (———) and linear instability theory of Mclean (1982) (- - -).

total disturbance:

$$R(t) \equiv \left\{ \frac{\displaystyle\iint_{\mathscr{F}} [\eta'(x, y, t)]^2 \, \mathrm{d}x \, \mathrm{d}y}{\displaystyle\iint_{\mathscr{F}} [\eta'(x, y, 0)]^2 \, \mathrm{d}x \, \mathrm{d}y} \right\}^{1/2}, \tag{5.3}$$

where $\mathscr{F}$ is the horizontal (periodic) domain. Figure 14 plots the time history of $R(t)$ from the simulation compared to the linearized theoretical result for the most unstable class II mode (Mclean 1982). The present fully nonlinear simulation result agrees very well with the prediction of the instability analysis. This supports the contention that crescent waves are a direct result of nonlinear wave evolution initiated by (class II) instability of Stokes wave in the absence of other physical effects.

The qualitative features in figures 11, 12 and 13 compare extremely well with observed crescent waves in experiments (e.g. figure 11 with figure 10 of Su 1982; and figure 13 with figures 13a, g, m of Su 1982). As an illustration, figure 15 compares a wave basin aerial photograph of a L_2 crescent wave (figure 17 of Su *et al.* 1982) with the simulated result in figure 11(h) (at $t/T \approx 5.641$). For the sake of comparison, the simulation result is rotated to match the perspective of the wave basin photograph. The resemblance is quite remarkable. The simulated L_2 crescent wave possesses all the notable features observed in the basin experiment, including the fully extended semi-circular crests, staggered row-shift crescent pattern, flattened troughs, rising Deltas, and steep crescent wave shoulders. Remarkably, although the (initial) disturbance in the simulation most likely differs from that in the physical experiment, the time durations required for the full development of the L_2 wave with the distinct crescent wave features in both simulation and experiment are quite close ($t/T \sim 5$).

We now turn to quantitative comparisons of the crescent wave features to experiments. Figure 16 shows longitudinal surface profiles (at $y = y_1$ and y_2 at $t/T = 4.338$) wherein the characteristic length and height parameters (according to Su 1982) are also labelled. Figure 16(a) shows typical L_2 feature of alternating peak and trough, while figure 16(b) on $y = y_2$ displays a (steepened) Stokes-wave-like regular profile.
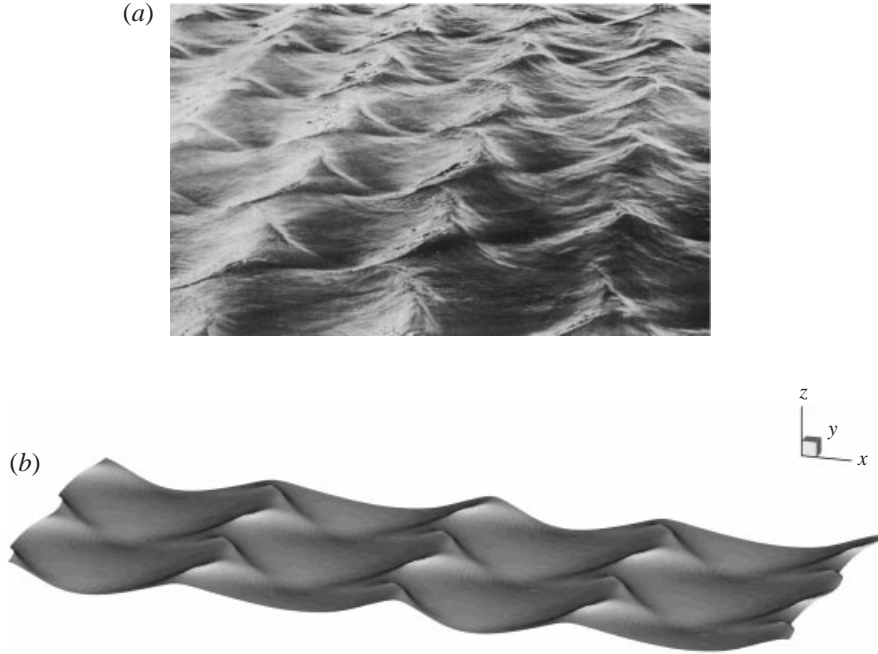
FIGURE 15. Comparison of an L_2 crescent wave train: (*a*) observed in a wave basin (figure 17 of Su *et al.* 1982, *reproduced with permission*); and (*b*) in simulation (at $t/T \approx 5.641$ cf. figure 11*h*).
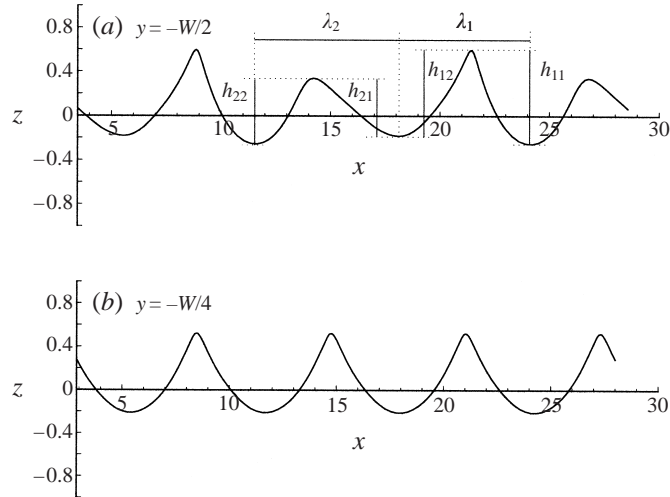

FIGURE 16. Longitudinal profiles of the L_2 crescent wave on the planes (*a*) $y = y_1$ and (*b*) y_2 at $t/T = 4.338$ obtained from simulation ($kA = 0.33$, $\epsilon = 0.16$, $\beta = 0$, and $(k_x, k_y) = (1.5, 1.23)$). Characteristic length and height parameters according to Su (1982) are labelled in (*a*).

These spatial variations are consistent with the observations made in figure 13 from the time histories.

Table 4 shows comparisons of the characteristic crescent wave geometric parameters at four representative times in the simulation with $t/T \in (3, 5)$ during which quasi-steady state approximately occurs. The agreements between simulation results and experimental measurements of Su (1982) are very good for the wave height ratios

	Experiment	Simulation			
	Su (1982)	$t/T = 3.171$	$t/T = 4.338$	$t/T = 4.955$	$t/T = 5.150$
λ_2/λ_1	1.28	1.05	1.07	1.03	1.17
h_{11}/h_{12}	1.10	1.18	1.09	1.18	1.26
h_{21}/h_{22}	0.88	0.81	0.88	0.80	0.75
h_{11}/h_{21}	1.66	1.49	1.64	1.63	1.60
s_{max}	0.65	0.45	0.64	0.69	0.51

TABLE 4. Comparisons of geometric parameters of L_2 crescent waves between the present simulation ($kA = 0.33$, $\epsilon = 0.16$, $\beta = 0$, and $(k_x, k_y) = (1.5, 1.23)$) and the experimental measurements of Su (1982).

h_{11}/h_{12}, h_{21}/h_{22}, and h_{11}/h_{21}, and the maximum local wave steepness s_{max}. The comparisons are particularly good at $t/T = 4.338$ and 4.955 when the L_2 crescent features are fully developed. The comparison of the wavelength ratio λ_2/λ_1 is acceptable but not as good as the other parameters. This is probably due to a lower accuracy in measuring wavelengths in the experiments.

5.2. *Dependence of L_2 crescent wave development on physical parameters*

We investigate the effects of the physical parameters of the problem on the development of the L_2 crescent waves.

As expected from physical reasoning, the precise phase β of the initial disturbance should have little effect on the eventual development of the L_2 wave. This is confirmed by direct simulation of the same problem ($kA = 0.33$, $\epsilon = 0.16$, $(k_x, k_y) = (1.5, 1.23)$) with $\beta = \pi/2$, which produces visually indistinguishable L_2 wave results from the earlier $\beta = 0$ case.

For a given Stokes wave steepness, kA, the initial disturbance amplitude ϵ can have a qualitative effect on the subsequent L_2 wave development. As expected, for relatively small kA (say 0.33 of §5.1), the effect of a smaller ϵ is merely to increase the evolution time for L_2 development. For steeper initial Stokes waves, however, the magnitude of ϵ can also change the nature of crescent wave breaking. Figure 17 shows the final stages of L_2 wave simulation for a larger $kA = 0.4$ with two different initial disturbance amplitudes ϵ. For a smaller value of $\epsilon = 0.04$, figure 17(*a*), the breaking at the crescent shoulder is that of wave spilling similar to that seen in §5.1. For a larger value of $\epsilon = 0.16$, figure 17(*b*), the breaking at the crescent is more characteristic of a plunging wave.

The longitudinal direction of propagation of the initial disturbance relative to the underlying Stokes waves has a strong effect on crescent wave formation. Results so far are for positive k_x (co-propagating disturbance and carrier waves). Figure 18 shows the growth rate $R(t)$ of an initial disturbance with negative $k_x = -1.5$ ($kA = 0.33$, $\epsilon = 0.16$, $k_y = 1.23$, $\beta = 0$). In contrast to figure 14 for positive $k_x = 1.5$, $R(t)$ for the counter-propagating disturbance displays similar (but slightly larger amplitude) oscillations but without increase in the mean value. The oscillation period is approximately $0.37T$ which corresponds to the encounter frequency of the disturbance moving on the carrier wave. Detailed analysis of the surface patterns in this case (not shown here, see Xue 1997 for details) shows that fully developed crescent waves do not form but rather the free surface displays a limit-cycle recurrence from almost two-dimensional to somewhat three-dimensional waves corresponding to the minima and maxima respectively of R in figure 18.
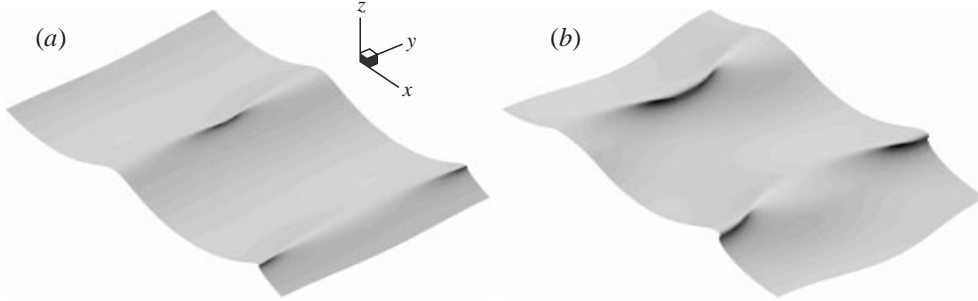
FIGURE 17. Differences in the L_2 crescent wave shoulder breaking pattern during the final stages of fully nonlinear simulation of a perturbed Stokes wave ($kA = 0.4$, $(k_x, k_y) = (1.5, 1.23)$, $\beta = 0$) and initial three-dimensional disturbance amplitude (a) $\epsilon = 0.04$; and (b) 0.16.
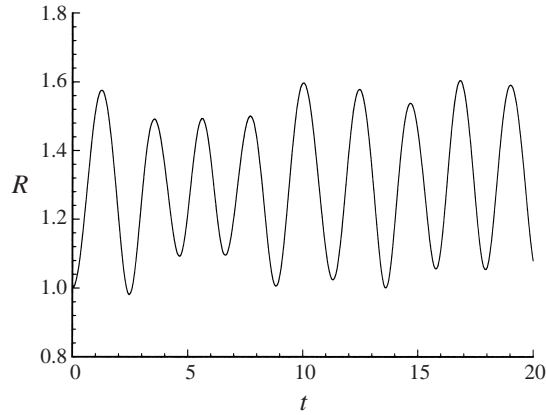

FIGURE 18. Growth rate $R(t)$ of the initial disturbance in the evolution of a perturbed Stokes wave ($kA = 0.33$, $\epsilon = 0.16$, $\beta = 0$, and $(k_x, k_y) = (-1.5, 1.23)$). The disturbance has a longitudinal propagation in a direction opposite to the Stokes wave.

In summary, it is seen that nonlinear evolutions of (linearly) unstable three-dimensional (class II) modes co-propagating on a steep Stokes wave train provide a sufficient and effective mechanism for the development of crescent waves under broad conditions.

5.3. L_3 crescent waves

In Su (1982), under natural conditions, it is reported that of the crescent waves observed, L_2, L_3 and L_4 configurations occur respectively approximately 90%, 10% and 1% of the time. The preceding results suggest that similar mechanisms can be employed to obtain these other crescent wave configurations.

As a demonstration, we obtain the L_3 crescent configuration by nonlinear simulation of a Stokes wave with initial three-dimensional disturbance corresponding to a (linearly) unstable sub-harmonic mode with $p = 1/3$ (i.e. $k_x = 4/3$). Figure 19 plots a representative stage in the development of L_3 crescent waves of such a case ($kA = 0.33$, $\epsilon = 0.12$, $(k_x, k_y) = (1.33, 1.23)$, $\beta = 0$). The three-row staggered structure of the L_3 crescent wave pattern is clearly shown, which compares well qualitatively to observations of such waves in the tank (e.g. Su 1982, figure 11). Our simulations indicate that, unlike the L_2 crescent pattern, such an L_3 pattern is non-stationary relative to the Stokes carrier. Furthermore, the L_3 configuration is characterized by
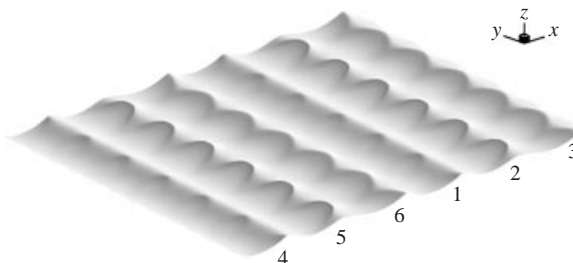
FIGURE 19. Free-surface wave pattern at $t/T = 4.198$ during the fully nonlinear evolution of a Stokes wave ($kA = 0.33$, $T = 5.951$) with an initial three-dimensional disturbance ($\epsilon = 0.12$, $(k_x, k_y) = (1.33, 1.23)$, $\beta = 0$). The consecutive crest rows corresponding to the original Stokes wave are labelled.

different crescent crest shapes at different rows. This is indicated by the 'high-high-low' (HHL) pattern of wave crest amplitudes in figure 19. All these features match well experimental observations of L_3 crescent waves (Su 1982).

6. Conclusions

We develop a mixed-Eulerian–Lagrangian method using a robust quadratic-boundary-element technique efficacious for the study of fully nonlinear three-dimensional wave–wave and wave–body interactions. Using this method, we investigate: (i) the nonlinear dynamics of three-dimensional plunging waves; and (ii) the mechanism for the formation of steep crescent waves. Wave–body interactions are described in the accompanying Part 2 of this work.

For three-dimensional breaking waves, we initially apply a free-surface pressure of transverse wavelength W on a Stokes wave of wavelength L, resulting, under broad conditions, in a three-dimensional plunging wave. We obtain simulations for a wide range of the three-dimensional parameter $\gamma \equiv W/L$ and quantify, as a function of γ, properties such as wave profiles, (surface) velocities and accelerations, and kinetic and potential energies.

Using direct simulations, we show that the nonlinear evolution of unstable three-dimensional (class II) disturbances on a steep Stokes wave leads to the development of characteristic crescent wave features. We obtain detailed descriptions of such waves which compare well qualitatively and quantitatively with experimental observations. The excellent comparisons rule out the necessity of physical effects other than those in the problem we consider.

Our study indicates that simulations are useful and practical for the understanding of three-dimensional fully nonlinear wave dynamics.

REFERENCES

BANNER, M. L. & PEREGRINE, D. H. 1993 Wave breaking in deep water. *Ann. Rev. Fluid Mech.* **25**, 373–397.

BANNER, M. L. & TIAN, X. 1998 On the determination of the onset of breaking for modulating surface gravity waves. *J. Fluid Mech.* **367**, 107–137.

BREIT, S. R. 1991 The potential of a rankine source between parallel planes and in a rectangular cylinder. *J. Engng Maths* **25**, 151–163.

DOLD, J. W. 1992 An efficient surface-integral algorithm applied to unsteady gravity waves. *J. Comput. Phys.* **103**, 90–115.

DOLD, J. W. & PEREGRINE, D. H. 1986 An efficient boundary-integral method for steep unsteady water waves. In *Numerical Methods for Fluid Dynamics II* (ed. K. W. Morton & M. J. Baines). Oxford University Press.

DOMMERMUTH, D. G., YUE, D. K. P., LIN, W. M., RAPP, R. J., CHAN, E. S. & MELVILLE, W. K. 1988 Deep-water plunging breakers: a comparison between potential theory and experiment. *J. Fluid Mech.* **189**, 423–442.

GREENHOW, M. 1983 Free-surface flows related to breaking waves. *J. Fluid Mech.* **134**, 259–275.

HAMMING, R. W. 1983 *Digital Filters*, 2nd edn. Prentice-Hall.

HESS, J. L. & SMITH, A. M. O. 1964 Calculation of potential flow about arbitrary bodies. *Prog. Aeronaut. Sci.* **8**, 1–138.

ISAACSON, M. DE ST.Q. 1982 Nonlinear-wave effects on fixed and floating objects. *J. Fluid Mech.* **120**, 267–281.

KINSMAN, B. 1984 *Wind Waves*. Dover.

LIN, W. M., NEWMAN, J. N. & YUE, D. K. P. 1984 Nonlinear forced motions of floating bodies. *Proc. 15th Symp. on Naval Hydrodynamics, Hamburg* (ed. O. Krappinger). Washington: National Academy Press.

LIU, Y., XUE, M. & YUE, D. K. P. 2001 Computation of fully nonlinear three-dimensional wave–wave and wave–body interactions. Part 2. Nonlinear waves and forces on a body. *J. Fluid Mech.* **438**, 41–65.

LONGUET-HIGGINS, M. S. 1996 Progress towards understanding how waves break. *Proc. 21st Symposium on Naval Hydrodynamics, Trondheim, Norway.* Washington DC: National Academy Press.

LONGUET-HIGGINS, M. S. & COKELET, E. D. 1976 The deformation of steep surface waves on water: I. A numerical method of computation. *Proc. R. Soc. Lond.* A **350**, 1–26.

LONGUET-HIGGINS, M. S. & COKELET, E. D. 1978 The deformation of steep surface waves on water, II. Growth of normal-mode instabilities. *Proc. R. Soc. Lond.* A **364**, 1–28.

LONGUET-HIGGINS, M. S. & DOMMERMUTH, D. G. 1997 Crest instabilities of gravity waves. Part 3. Nonlinear development and breaking. *J. Fluid Mech.* **336**, 33–50.

McLEAN, J. W. 1982 Instabilities of finite-amplitude water waves. *J. Fluid Mech.* **114**, 315–330.

MEIRON, D. I., SAFFMAN, P. G. & YUEN, H. C. 1982 Calculation of steady three-dimensional deep-water waves. *J. Fluid Mech.* **124**, 109–121.

NEW, A. L., McIVER, P. & PEREGRINE, D. H. 1985 Computations of overturning waves. *J. Fluid Mech.* **150**, 233–251.

NEWMAN, J. N. 1992 The Green function for potential flow in a rectangular channel. *J. Engng Maths* **26**, 51–59.

RAPP, R. J. & MELVILLE, W. K. 1990 Laboratory measurements of deep-water breaking waves. *Phil. Trans. R. Soc. Lond.* A **331**, 735.

ROMATE, J. E. 1989 The numerical simulation of nonlinear gravity waves in three dimensions using a higher panel method. PhD thesis, University of Twente, Enschede, The Netherlands.

SAAD, Y. & SCHULTZ, M. H. 1986 GMRES: A generalized minimal residual algorithm for solving nonsymmetric linear systems. *SIAM J. Sci. Statist. Comput.* **7**, 856–869.

SAFFMAN, P. G. & YUEN, H. C. 1980 A new type of three-dimensional deep-water wave of permanent form. *J. Fluid Mech.* **101**, 797–808.

SCHULTZ, W. W., HUH, J. & GRIFFIN, O. M. 1994 Potential energy in steep and breaking waves. *J. Fluid Mech.* **278**, 201–228.

SCHWARTZ, L. W. 1974 Computer extension and analytic continuation of Stokes' expansion for gravity waves. *J. Fluid Mech.* **62**, 553–578.

SHRIRA, V. I., BADULIN, S. I. & KHARIF, C. 1996 A model of water wave 'horse-shoe' patterns. *J. Fluid Mech.* **318**, 375–404.

SNYDER, R. L. & KENNEDY, R. M. 1983 On the formation of whitecaps by a threshold mechanism. Part I: basic formalism. *J. Phys. Oceanogr.* **13**, 1482–1492.

SU, M.-Y. 1982 Three-dimensional deep-water waves. Part I. Experimental measurement of skew and symmetric wave patterns. *J. Fluid Mech.* **124**, 73–108.

Su, M.-Y., Bergin, M., Marler, P. & Myrick, R. 1982 Experiments on nonlinear instabilities and evolution of steep gravity-wave trains. *J. Fluid Mech.* **124**, 45–72.

Tsai, W. T. & Yue, D. K. P. 1996 Computation of nonlinear free-surface flows. *Ann. Rev. Fluid Mech.* **28**, 249–278.

Vinje, T. & Brevig, P. 1981 Numerical simulation of breaking waves. *Adv. Water Resour.* **4**, 77–82.

Wang, P., Yao, Y. & Tulin, M. P. 1994 Wave group evolution, wave deformation, and breaking: simulations using LONGTANK, a numerical wave tank. *Intl. J. Offshore Polar Engng* **43**, 200–205.

Xü, H. 1992 Numerical study of fully nonlinear water waves in three dimensions. PhD thesis, Massachusetts Institute of Technology, USA.

Xü, H. B. & Yue, D. K. P. 1992 Computations of fully-nonlinear three-dimensional water waves. In *Proc. 19th Symposium on Naval Hydrodynamics, Seoul, Korea.* Washington DC: National Academy Press.

Xue, M. 1997 Three-dimensional fully-nonlinear simulations of waves and wave body interactions. PhD thesis, Massachusetts Institute of Technology, USA.

Yao, Y., Wang, P. & Tulin, M. P. 1994 Wave groups, wave-wave interactions and wave breaking: results of numerical experiments. In *Proc. 20th Symp. on Naval Hydrodynamics, Santa Barbara, USA.*